0.13μm CMOS 230Mbps 21pJ/b UWB-IR Transmitter with 21.3% Efficiency

Nima Soltani, Hossein Kassiri, Hamed M. Jafari, Karim Abdelhalim, Roman Genov
Email: {nima, roman}@eecg.utoronto.ca
Department of Electrical and Computer Engineering,
The University of Toronto, Toronto, Ontario M5S 3G4, Canada

***Abstract*—An ultra-wide-band impulse-radio (UWB-IR) transmitter for low-energy implantable and wearable biomedical microsystems is presented. The transmitter provides a power-efficient high-data-rate wireless link within the 3-5 GHz band. It yields an overall power efficiency of 21.3% at data-rate of 230Mbps while consuming 21pJ per bit. The transmitted UWB pulse train is recovered at the receiver with less than 10^{-6} bit-error-rate (BER) measured at a distance of 1m without any pulse averaging. The chip is implemented in a 130nm CMOS technology and has an average power consumption of 3.7mW.**

I. Introduction

Short-range wireless transmission is critical to implantable and wearable biomedical devices such as retinal prosthetic implants [1], responsive neuro-stimulation systems [2], and high-throughput DNA sequencing microarrays [3]. With the ever increasing size of sensor array and the improved resolution of each sensing element, modern implantable and wearable devices require more bandwidth to transmit the resulting data.

Ultra-wideband impulse radio (UWB-IR) is one of the most suitable architectures for short-range (<10m) medium data-rate (>10Mb/s) transmission [4], [5]. A UWB-IR transmitter (TX) directly radiates a train of short pulses (<1ns) each typically representing one symbol. The direct transmission of impulses results in high data-rates as the symbol period can be nearly as small as duration of the individual impulses. Compared with the state-of-the-art in low-power narrow band transmitters [6], [7], UWB-IR transmitters offer ×10 or more bandwidth and reduced per-bit energy dissipation [5], [9], [10].

The high bandwidth of the UWB-IR TX, however, comes at the cost of reduced TX power efficiency. Compared with the latest narrow band TXs , UWB-IR TXs typically are at least ×4 [5]–[10] less power efficient. The reduced power efficiency of the UWB-IR TX can generally be attributed to poor efficiency of the output stage which drives the antenna [4]. Unlike narrow-band transmitters which take advantage high-efficiency switching power amplifier (PA) [11], a UWB-IR TX cannot use a switching PA (such as a class D). This is because the main component of the switching PA, the passive narrow band filter, would block the UWB impulses entirely.

There are several innovative low-power UWB-IR architectures proposed for biomedical wearable and implantable devices [3]–[5], [9], [12], [13]. The design in [5] uses a combination of inverters to generate the UWB waveform and drive the antenna. The TX only radiates power during the logic-state transitions. The TX efficiency is therefore limited by that of a CMOS inverter during rise and fall times which is limited to 50% in the ideal case. In practice, due to the added consumption in the digital delay-lines and other pulse-shaping circuits, the design yields an overall power efficiency of approximately 21.3%. The designs in [4], [14], [15] generate UWB pulses by turning on and off a digitally-controlled cross-coupled LC oscillator. The TX efficiency performance therefore depends on the efficiency of the CMOS oscillator during startup period. Power efficiency, however, is poor during startup time as oscillation swing is small, and slowly increases to its maximum value in the steady state, before which point the pulse period is over and the tank is switched off. On the other hand, if the UWB pulses are generated from an LC tank in steady state, the efficiency of the tank can be maintained. Moreover, because all the pulse power is sourced from the tank, the overall efficiency of the UWB-IR transmitter can also be expected to remain high at all times.

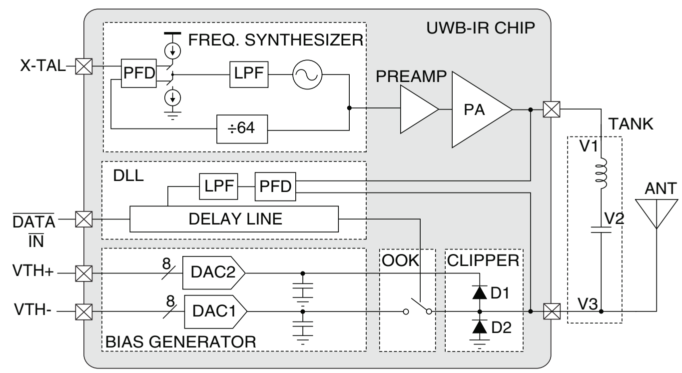

Fig. 1. Block diagram of the proposed UWB-IR transmitter.

This paper proposes a new high-efficiency UWB-IR TX architecture by introducing a non-linearity at the output of a resonant LC tank driven by a class C PA. The proposed TX generates pulses by introducing a non-linearity at the output of the LC tank resonating in steady state. Fig. 2 shows the schematic of the proposes UWB-IR transmitter. By drawing all the pulse power from the LC tank in steady-state, this UWB-IR TX provides an overall efficiency of 21.3% at data-rate of 230Mb/s.

II. System Architecture

Fig. 1 shows the block diagram of the proposed UWB-IR transmitter including a 915MHz frequency synthesizer, amplifiers, resonant LC tank, 2-diode clipper circuit and delay-locked loop (DLL) for pulse on-off keying (OOK) modulation. Fig. 2 shows conceptual diagrams of UWB pulse generators using the conventional and the proposed schemes. In the conventional TX (Fig. 2(a)), pulses are created by switching on and off an LC tank oscillator. In the proposed UWB pulse generation circuit (Fig. 2(b)), the LC tank is always in steady-state and 2 UWB pulse are generated in every oscillation period. The high bandwidth pulses are generated by clipping the output of the LC tank with a diode-connected NFET pair.

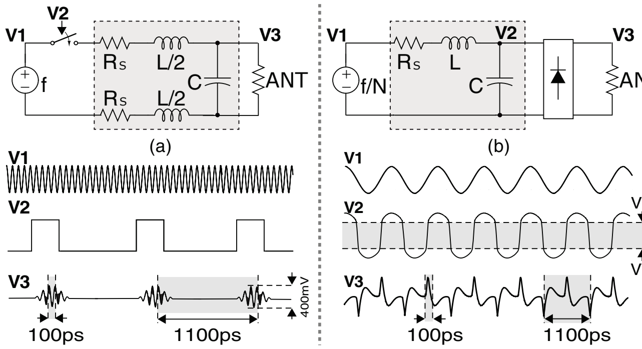

Fig. 2. (a) Convetional and (b) proposed pulse generation using LC tank.

A 915MHz pure tone is generated by an on-chip frequency synthesizer from an off-chip 14.3MHz crystal. The synthesizer is connected to a preamplifier which drives an inductive load power amplifier (PA), which in turn drives a high-Q off-chip series LC tank. The diode clipper is implemented with diode-connected triple-well devices at DC voltages V_{TH} and $V_{TH}-$ set by DAC1 and DAC2.

The inductor in Fig. 2(b) has high quality factor and large voltage swing which is not readily available in an integrated spiral inductor due to the high substrate loss. The swing at the output node of the tank ,V_2, is clipped between two DC levels by the two diode-connected NFET devices. The clipped signal, V_2, contains higher order harmonics in due to the abrupt limiting action of the diodes. As shown in Fig. 2, the raw UWB pulsetrain (V_3) is created at the input of the antenna (V_2) by blocking the low-frequency components of the clipped signal using a high-pass L network. The clipping threshold levels $V_{TH}+$ and $V_{TH}-$ are determined by two 8-bit DACs. Adjusting the inputs of DAC1 and DAC2, the threshold levels for maximum radiated power can be found digitally.

Data stream modulates the UWB pulsetrain by switching the tank output to the AC ground set by DAC1. By shorting V_2 to ground during D1 and D2 transitions, both diodes remain off, therefore no pulse is generated. The switch, however, does not impact the quality of the tank resonance since the swing of V_2 still remains many times smaller than the swing of V_1 regardless of the switch state. A delay-locked loop (DLL) is situated between the data stream and the switch node to ensure proper timing between of the switching signal and diodes transitions. The DLL ensures that the switch signal precedes the next oscillation cycle of the tank by $T/4$, where T is the period of tank, approximately equal to $1.1ns$ (also shown in Fig. 4).

III. Circuit Implementation

The impulse-radio transmitter is designed in standard $0.13\mu m$ CMOS technology. The frequency synthesizer is designed with a conventional cross-coupled LC tank VCO and TSPC flip-flop phase-frequency detector. Design of proposed pulse generation and the delay-locked loop for OOK pulse modulation circuit is discussed here.

A. Pulse Generation

Fig. 3 shows the schematic diagram of the pulse generation circuit including the pre-amplifiers, power amplifier, LC tank, diode clippers and the OOK switch. The preamplifier is a self-biased differential pair with current mirror biasing for the tail current device M1. The power amplifier is a common-source

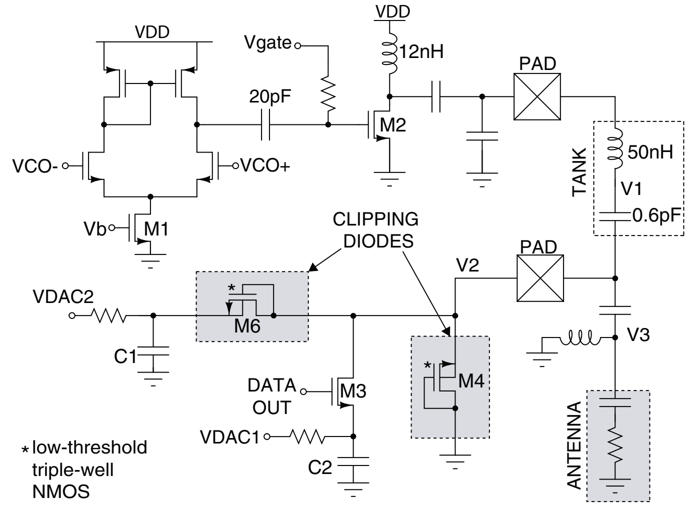

Fig. 3. Pulse generator schematic.

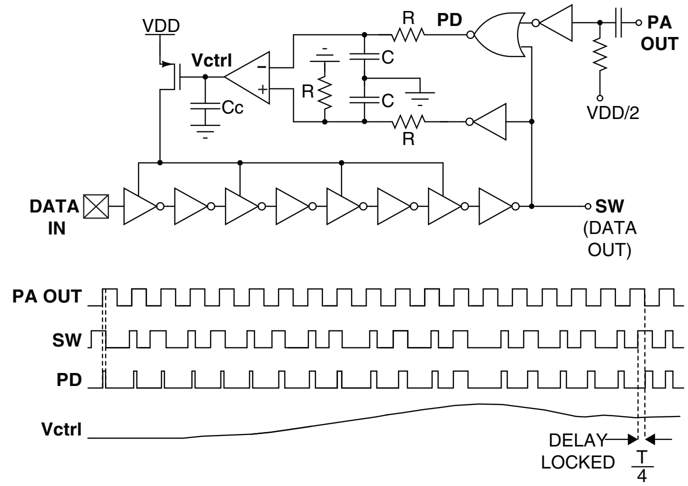

Fig. 4. Delay-locked loop schematic for OOK modulation.

stage with inductive load biased as a class C amplifier.

The clipping diodes are each implemented by two series diode-connected MOSFET devices (M4&M5, and M6&M7). All the diode-connected devices have a width of $50\mu m$ and minimum length. The OOK switch is implemented by the NMOS device M3 which has minimum length and a width of $200\mu m$.

To set the DC threshold voltages $V_{TH}+$ and $V_{TH}-$, large capacitors C_1 and C_2 are used as decoupling capacitors at output voltages of DAC1 and DAC2. $C_{1,2}$ are implemented with banks of poly capacitors each with total capacitance of $200pF$. Capacitor C_1 sets the high clipping threshold $V_{TH}+$ while C_2 sets the low threshold by offsetting the tank AC ground by $V_{TH}-$.

B. OOK Pulse Modulation

Fig. 4 shows the schematic of the delay-locked loop circuit used to properly align the data stream bits with the tank oscillation cycles. The loop regulates the delay of a variable inverter-chain delay line until the output of the delay line and the PA are misaligned by exactly $T/4$ with the latter rising edge preceding, where T is the tank oscillation period. The DLL quantifies the misalignment between the two rising edges

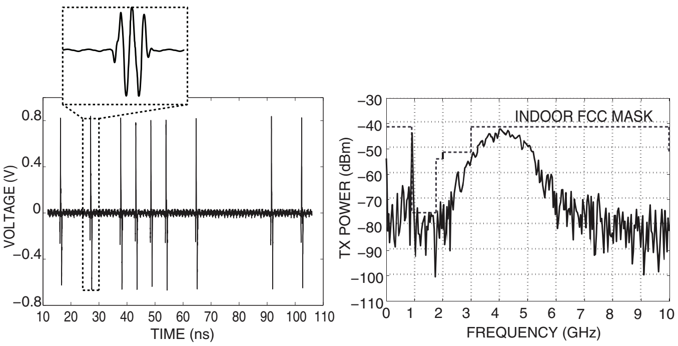

Fig. 5. Experimentally measured modulated time domain output of the transmitter (left), and power spectrum (right).

by comparing the duration of each ”1” bit with the duration of the ”1” bit concurring with the PA output being positive. For this, the PA output is digitized to a squarewave using an inverter with AC-coupled input, as shown in Fig. 4. The digitized PA output is ANDed with the data bits at the output of the delay line. Two pulse-averaging RC filters quantify the pulsewidths of the data ”1” bits as seen at the output of the delay line and the bits ANDed with PA output. The RC filter averaging the ANDed bits has a DC weight of 1/2, such that the two filters have equal output levels when the PA and data signals are exactly a quarter of a period apart. The phase difference between the two edges is quantified by a differential amplifier which is implemented as a self-biased differential pair. Compensation capacitor C_c is added to the differential amplifier output to stabilize the feedback loop.

As shown in the timing diagram of Fig. 4, an axillary quarter-period ”1” bit follows every data bit to ensure that the loop settle only when the bits *precede* the PA zero crossings by a $T/4$. Without the axillary ”1” bit, the DLL may just as likely settle when the bits *follow* the PA output by a $T/4$.

IV. Experimental Results

The output of the transmitter is measured by an Agilent DSO-X 92004A realtime oscilloscope, sampling at 80GSa/s. Fig. 5 is the measured transient unmodulated output of the transmitter at the maximum output power. Low frequency components of the TX output waveform are further suppressed by the high-pass characteristics of the antenna feedline.

Fig. 5(left) shows the transient output of the transmitter modulated by a pseudorandom binary sequences(PRBS). Fig. 5(right) is the spectrum of the OOK modulated pulse train. It spreads over the 3-5GHz frequency range. At higher UWB frequencies the antennas either have smaller aperture or are extremely sensitive to misalignment. Therefore extending radiated spectral power beyond this range is of less interest, especially for biomedical wearable and implantable sensor applications where the misalignment of the antennas often cannot be avoided.

The transmitted pulses are detected using a receiving (RX) antenna connected to the Agilent DSO-X 92004A with deep memory acting as detector. The scope is set to be triggered by any notch in the received signal that is smaller than 500ps wide. The scope setup is such that once a notch is detected, a 10ns segment of the recorded RX signal containing the notch is stored in the scope memory. All the stored RX segments are later processed offline (in a computer) to determine bit error rate. The computer performs a correlated double sampling

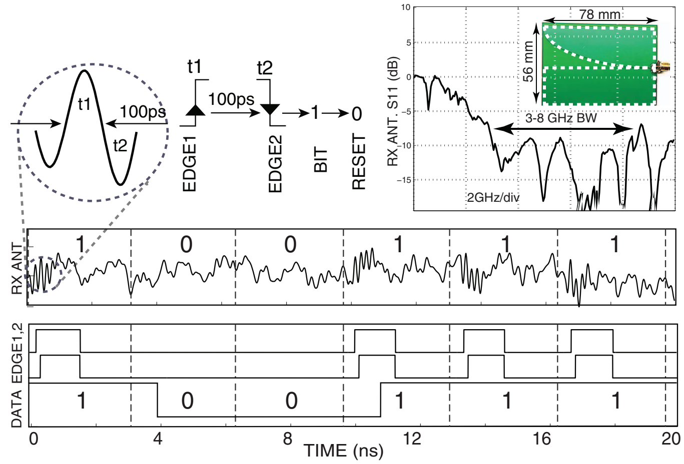

Fig. 6. Receiving antenna return loss, and experimentally measured output of the receiving antenna by oscilloscope (Agilent DSO-92004) (top), rise and fall edges, and data stream detected by computer algorithm processing the RX antenna signal.

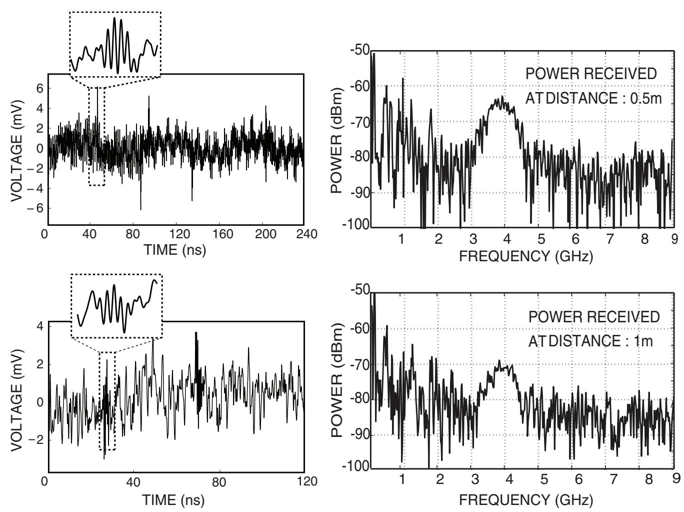

Fig. 7. Experimentally measured received UWB signal by antenna at 50cm (top) and 1m (bottom).

scheme as shown in Fig. 6 (top). By taking three consecutive samples from the RX signal in 100ps intervals, the algorithm detects where a transmitted pulse exists within each stored segment of the scope.

The receiver recovers the pulses by interpreting the results according to the scheme in Fig. 6(top). The Fig. 6 (bottom) shows the combined output of the two detectors based on the detection scheme in Fig. 6 (top). The “EDGE1, $\overline{2}$” signal is the outputs of two slope detection blocks within the algorithm which evaluate the rise in amplitude from $t0$ to $t1$, and from $t1$ to $t2$ respectively. A UWB pulse is flagged to be present within the segment when the output of both slope detectors “EDGE1” and “EDGE, $\overline{2}$” are high. A bit ”1” is assigned to each recorded RX segment when the algorithm detects a UWB pulse within that segment. Each segment also has a time stamp recorded within using a separate channel. By comparing the bit ”1” segments with the original transmitted PRBS sequence, the BER is estimated. A bit ”0” is assumed for at all times where no pulse is detected by the algorithm. Fig. 7 shows

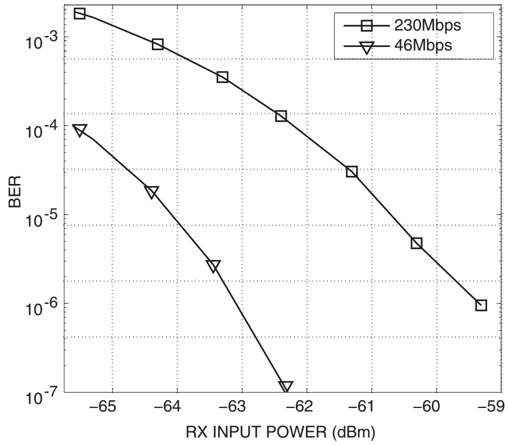

Fig. 8. Experimentally measured TX-RX bit error rate.

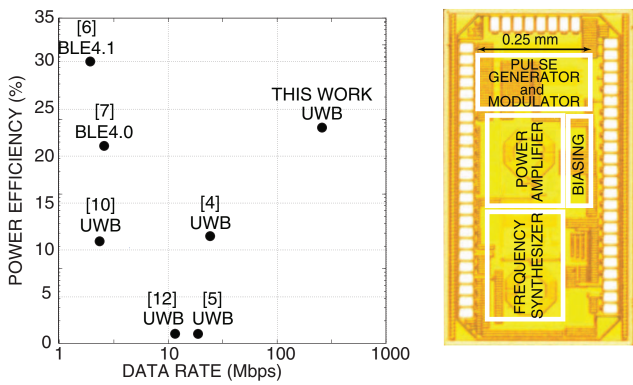

	[5] JSSC'09	[10] TCASI'12	[12] VLSI'12	[4] ESSCIRC'14	THIS WORK
TECHNOLOGY	90 nm CMOS	130 nm CMOS	90 nm CMOS	130 nm CMOS	130 nm CMOS
AREA(mm^2)	0.07	0.23	0.37	0.5	0.48
SUPPLY(V)	1	0.5-1.2	1	0.5	1.2 / 3.3
BANDWIDTH(GHz)	2	0.5	1	1.25	2
MODULATION	PPM+BPSK	OOK	8-PPM	PPM	OOK
AVG POWER(mW)	4.36	0.0007	0.54	0.47	3.7
P_{OUT} (dBm)	**-16.4**	**-**	**-26**	**-12.6**	**-1**
DATA RATE(Mbps)	**15.6**	**0 - 5**	**12**	**20**	**230/46**
TX EFFICIENCY (%)	**0.5**	**10.6**	**0.46**	**11.7**	**21.35**
ENERGY/BIT(PJ)	**17.5**	**32**	**45**	**2.76**	**21**

Fig. 9. Die micrograph and performance summary of the transmitter.

signal received by the antenna at 50cm (top, left) and 100cm (bottom, left) distances from the transmitter. Power spectra of the signals are shown on the right, respectively. At distances greater than 120cm, a 5-pulse averaging scheme in conjunction with the double-sampling scheme in Fig. 6(a), in used to recover attenuated UWB pulses at distances of up to 2m.

The measured BER performance of the transmission system is plotted in Fig. 8 for two different transmission data rates: 230Mbps which is equal to the pulse rate of the transmitter, and 46Mbps when a 5-pulse averaging scheme is applied whereby 5 pulses are transmitted to represent a bit. The die micrograph and comparative analysis of the UWB-IR transmitter are shown in Fig. 9. As compared with the state of the art, this design offers significantly improved overall power efficiency of 21.3% at TX data-rate of 230Mb/s using the proposed pulse generation from a continuously resonating LC tank.

V. Conclusion

A power efficient resonant tank UWB-IR transmitter for biomedical wearable and implantable sensory microsystems is presented. The proposed transmitter significantly improves overall power efficiency a TX data-rate of 230Mb/s with 21pJ/b power consumption. The experimental results shows transmission BER of less than 10^{-6} at 46Mbps over a 2m distance from the receiver, and 230Mbps over a 1m distance from the receiver.

References

[1] Y. Liu, *et al*, "Wireless goggles for near-infrared fluorescence and real-time image-guided surgery", *Surgery*, vol. 149, vol. 5, 689–698, 2011.

[2] H. Kassiri, et al "Inductively-Powered Direct-Coupled 64-Channel Chopper-Stabilized Epilepsy-Responsive Neurostimulator with Digital Offset Cancellation and Tri-Band Radio," IEEE ESSCIRC Dig. Tech. Papers, Sept. 2014, pp. 95–98.

[3] H. Jafari, et al., "Nanostructured CMOS wireless ultra-wideband label-free DNA analysis SoC," ESSCIRC, pp. 122–123, Jun. 2012.

[4] F. Padovan, A. Bevilacqua, and A. Neviani, "A 20Mb/s, 2.76 pJ/b UWB impulse radio TX with 11.7% efficiency in 130 nm CMOS," in Proceedings of the 2014 ESSCIRC, 2014.

[5] P. Mercier, D. Daly, and A. Chandrakasan, "An energy-efficient alldigital UWB transmitter employing dual capacitively-coupled pulseshaping drivers," IEEE Journal of Solid-State Circuits, vol. 44, no. 6, pp. 1679–1688, Jun. 2009.

[6] Liu, Yao-Hong, et al. "A 3.7 mW-RX 4.4 mW-TX fully integrated Bluetooth Low-Energy/IEEE802. 15.4/proprietary SoC with an ADPLL-based fast frequency offset compensation in 40nm CMOS," ISSCC Dig. Tech Papers, pp. 236–237, Feb. 2015.

[7] A. Wang, et al., "A 1V 5mA Multimode IEEE 802.15.6/Bluetooth Low-Energy WBAN Transceiver for Biotelemetry Applications," ISSCC Dig. Tech Papers, pp.300–301, Feb. 2012.

[8] J. K. Brown *et al.*, "An Ultra-Low-Power 9.8 GHz Crystal-Less UWB Transceiver with Digital Baseband Integrated in 0.18 μm BiCMOS," *ISSCC*, pp. 42–443, Feb. 2013.

[9] Y. Park and D. D. Wentzloff, "An all-digital 12 pJ/Pulse IR-UWB transmitter synthesized from a standard cell library," IEEE Journal of Solid-State Circuits, vol. 46, no. 5, pp. 1147–1157, May 2011.

[10] M. Crepaldi et al., "A very low-complexity 0.3 4.4 ghz 0.004mm2 all-digital ultra-wide-band pulsed transmitter for energy detection receivers," IEEE Transactions on Circuits and Systems I: Regular Papers, vol. 59, no. 10, pp. 2443–2455, Oct 2012.

[11] S. C. Cripps, RF Power Amplifiers for Wireless Communication. Norwood, MA: Artech House, 1999.

[12] V. Majidzadeh et al., "An 8-PPM, 45 pJ/bit UWB transmitter with reduced number of PA elements" *VLSI Symposium*, pp. 36–37, Jun. 2012.

[13] J. Mao, Z Zou, Li. Zheng, "A 35 pJ/pulse injection-locking based UWB transmitter for wirelessly-powered RFID tags," *ESSCIRC*, pp. 379–382, Sep. 2013.

[14] F. Chen, Y. Li, D. Liu, W. Rhee, J. Kim, D. Kim, Z. Wang "A 1mW 1Mb/s 7.75-to-8.25GHz chirp-UWB transceiver with low peak-power transmission and fast synchronization capability," *ISSCC*, pp. 162–163, Feb. 2014.

[15] S. Geng, et al., "A 13.3mW 500Mb/s IR-UWB transceiver with link margin enhancement technique for meter-range communications," in the proceeding of IEEE ISSCC Dig. Tech. Papers, Feb. 2014.